Chemical Engineering Journal 515 (2025) 163102

Contents lists available at ScienceDirect

Chemical Engineering Journal

journal homepage: www.elsevier.com/locate/cej

Novel six flux model two-dimensional (SFM-2D) approach for evaluation of radiation field in slurry photocatalytic reactors with rectangular flat slab geometries☆

Clovis Nchikou [a], José Ángel Loredo-Medrano [a], Aracely Hernández-Ramírez [a], José Ángel Colina-Marquez [b], Miguel Ángel Mueses [b,*], Gianluca Li Puma [c,*]

[a] Universidad Autónoma de Nuevo León, UANL, Facultad de Ciencias Química, Av. Universidad s/n, Cd. Universitaria, C.P. 6645 San Nicolás De Los Garza, Nuevo León, Mexico

[b] Photocatalysis & Solar Photo-Reactors Engineering, Modeling & Application of Advanced Oxidation Processes, Chemical Engineering Department, Universidad de Cartagena, A. A. 1382 - Postal 195, Cartagena, Colombia

[c] Environmental Nanocatalysis & Photoreaction Engineering, Department of Engineering, University of Palermo (UNIPA), Palermo, Italy

ARTICLE INFO

Keywords:
Radiation transfer
Photocatalyst suspension
Photoreactor modeling
TiO_2-P25
Reactor optimization

ABSTRACT

The radiative transfer equation (RTE) in slurry photocatalytic reactors with flat-slab geometries was solved analytically through a new two-dimensional Six-Flux Model approach (SFM-2D), which overcomes the limitations of the SFM and SFM-HG approaches regarding long photon pathways and non-uniform radiation distributions on the front wall of the slab. The model builds a set of partial differential equations of photon balances solved by combining different mathematical methods and suitable boundary conditions, and yields an analytical solution of the local volumetric rate of photon absorption (LVRPA). The model also allows for radiation absorption by the suspended photocatalytic particles and by the fluid matrix, including all reactive species. The radiant field of a flat plate photocatalytic reactor using the proposed model was compared with the SFM-HG approach, using both constant and variable incident radiation boundary conditions. The LVRPA profiles calculated with the SFM-2D and the SFM-HG matched closely in the region near the slab front wall where the incident radiation source enters the reactor, but were significantly different in the regions far away from it. The SFM-2D provides a more accurate optimization of the radiation field in a flat plate with non-uniform irradiation of the front wall, allowing a more accurate estimation of the optimum catalyst load and slab thickness, thus facilitating the design of photocatalytic reactors with suspended photocatalysts.

1. Introduction

Photocatalytic reactors are a class of chemical reactors which have application in the environmental sector such as water or air decontamination [1,2], in the renewable energy sector, such as water splitting, hydrogen production or photo-reforming of chemical species [3,4], and also in the synthesis of chemicals by partial oxidation [5,6]. This class of reactors incorporates a light-activated photocatalyst in either supported or suspended form. The light usually enters from a reactor boundary, i.e., a free fluid surface or a transparent reactor wall. Undoubtedly, the key feature that distinguishes photocatalytic reactors from chemical reactors is the presence of light waves, and of an irreducible heterogeneous radiation field which needs to be determined to evaluate the rate of reaction of the reacting species within the photocatalytic reactor. Essentially, the design, modeling, and optimization of such reactors require the evaluation of the local volumetric rate of photon absorption (*LVRPA*) (Eq. (1)), which is the rate of radiant energy absorbed by the photocatalyst at a specific position in the reactor. The *LVRPA* is required for the evaluation of the reaction rates of the reactive species, which are position-dependent in the reactor.

$$LVRPA = \int_{\Omega}\int_{\lambda} k_{\lambda} \mathrm{I}_{\lambda} d\lambda d\Omega \tag{1}$$

The evaluation of the *LVRPA* depends on the solution of the radiative

☆ This article is part of a special issue entitled: 'Dion Dionysiou Memorial Issue' published in Chemical Engineering Journal.

* Corresponding authors.
E-mail addresses: mmueses@unicartagena.edu.co (M.Á. Mueses), gianluca.lipuma@unipa.it (G. Li Puma).

https://doi.org/10.1016/j.cej.2025.163102

Available online 30 April 2025

transfer equation (RTE) (Eq. (2)) that governs the distribution of radiant energy in the photocatalytic reactor:

$$\frac{dI_\lambda(S,\Omega)}{ds} = -k_\lambda I_\lambda(S,\Omega) - \sigma_\lambda I_\lambda(S,\Omega) + \frac{\sigma_\lambda}{4\pi}\int_{\Omega=4\pi} P(\Omega'\rightarrow\Omega) I_\lambda(S,\Omega')d\Omega' \quad (2)$$

where I_λ is the photon irradiance (W/m^2), k_λ the absorption coefficient (m^2/kg), σ_λ the scattering coefficient (m^2/kg), $P(\Omega'\rightarrow\Omega)$ the scattering phase function, λ the wavelength (m), S the spatial coordinate (m), and Ω the directional solid angle (steradian) [7,8,9].

The mathematical structure of this integral–differential equation makes its solution a challenging task. Previous studies have focused on the numerical solution of the RTE, using methods such as Monte Carlo (MC) and Discrete Ordinates Method (DOM) [10,11] and on the development of simplified models such as the six-flux model (SFM), yielding an analytical solution of the RTE [12]. Simplified modeling approaches are very attractive since they facilitate the design and optimization of photocatalytic reactors without the need to perform lengthy and costly numerical calculations, particularly in reactors with fluctuating incident photon fluxes such as solar light. For example, the SFM facilitates the optimization of solar photocatalytic reactors through the selection of optimal catalyst concentration and reactor geometry based on the well-established concept of *optimum optical thickness* [13,14,15].

The SFM originally developed over a slab geometry with a suspended photocatalyst [12], referred here as SFM-1D, stipulates that a photon, after colliding with a suspended particle, can be reflected (or scattered) along the six directions of the Cartesian coordinates with a well-defined probability. This approach demands less computational time and effort and returns minor significant discrepancies compared to more complex numerical solutions of the RTE, such as DOM [12,16]. Nonetheless, the SFM-1D assumes infinite reactor dimensions along two axes of the slab. One of the main conceptual limitations of the SFM-1D is its sequential assumption of infinite planes to describe the bidirectional behavior of the photon path [17]. This results in a poor representation of deep reactors, limiting the model's applicability to real systems (e.g., raceway reactors [18,19]). The SFM-1D analytical solution of the *LVRPA* is limited to one dimension (the reactor depth); it neglects the absorption of radiation by the fluid matrix and considers that the incident radiation flux at the front reactor window remains constant [12]. Such restrictive assumptions can limit the design of practical photocatalytic reactors using suspended photocatalysts. For example, it is common to have incident radiation varying along the boundary of a slab geometry. Just imagine using heterogeneous photocatalysis for water treatment at a laboratory scale using a cylindrical lamp to illuminate a flat plate reactor or, for the same purpose, a water treatment plant using solar panels emitting radiation varying from one point to another point on the reactor wall. In these cases, solving the RTE in two or three dimensions is required.

To overcome these limitations, this study proposes a solution for the RTE over two dimensions in rectangular coordinates through the formulation of a new two-dimensional six-flux model approach (SFM-2D), which yields an analytical solution of the *LVRPA* describing the radiant field in slabs photoreactor geometries. Variable photon flux boundary conditions along one dimension of the front wall were included in the model solution. The model also allows for radiation absorption by the suspended photocatalytic particles and by the fluid matrix, including all reactive species. The proposed mathematical formulation and structure ensure a more accurate description of the photon path, even in planar geometries with significant depth or high optical thickness. From a computational perspective, it is well known that analytical solutions, such as the SFM-1D, ensure low computational times and reduce the need for high-end processors, which are typically required for computational packages in photonic CFD simulations or methods like the discrete ordinate and Monte Carlo approaches [20,21]. The validation of the SFM-2D model and its easy implementation as an algebraic model in its final structure allows it to serve as a heuristic tool for real systems, facilitating the design and engineering calculations of solar photoreactors used in water treatment and decontamination [22]. Overall, this study demonstrates that the SFM-2D provides a more accurate optimization of the radiation field in a flat plate and allows a more accurate selection of the optimum catalyst load and slab thickness, facilitating the design of photocatalytic reactors with suspended photocatalysts.

2. Materials and methods

2.1. Six-flux model in rectangular coordinates in 2D

The SFM-2D was formulated to derive the *LVRPA* in rectangular coordinates, following the more general approach of Clovis Nchikou et al., (2021) [23] considering the absorption of radiant energy by both: the fluid matrix (including all dissolved and reacting species) and by the suspended photocatalyst. Likewise the original SFM, the SFM-2D supposes that photons are scattered only along the six directions of the Cartesian coordinates, which are set as shown in Fig. 1. The SFM-2D used here relies on the following assumptions:

- An infinitely wide slab of thickness L
- Geometric optics holds (hence, large and largely spaced particles)
- Random particles are homogeneously distributed inside the space
- The fluid matrix may absorb radiation
- When a photon hits a particle, only scattering or absorption occurs (no radiation emission); the scattering probability is given by the catalyst albedo ω
- The scattering event can occur only along the six directions of the Cartesian coordinates

For symmetry considerations, the probability of sidewise scattering s along any of the four directions of the plane (z-y) normal to the incident light is the same, while the forward f and backward b scattering probabilities may differ. The analytical expression of the *LVRPA* was formulated by performing the energy balance over a differential control volume of the slab (Fig. 1 and Supporting Information (SI)). Thus:

$$\frac{\partial(E_1)}{\partial x} = \frac{1}{\lambda_0}[(-1+\omega f)E_1 + \omega b E_2 + \omega s(E_3+E_4+E_5+E_6)] \quad (3)$$

$$\frac{\partial(E_2)}{\partial x} = \frac{1}{\lambda_0}[(+1-\omega f)E_2 - \omega b E_1 - \omega s(E_3+E_4+E_5+E_6)] \quad (4)$$

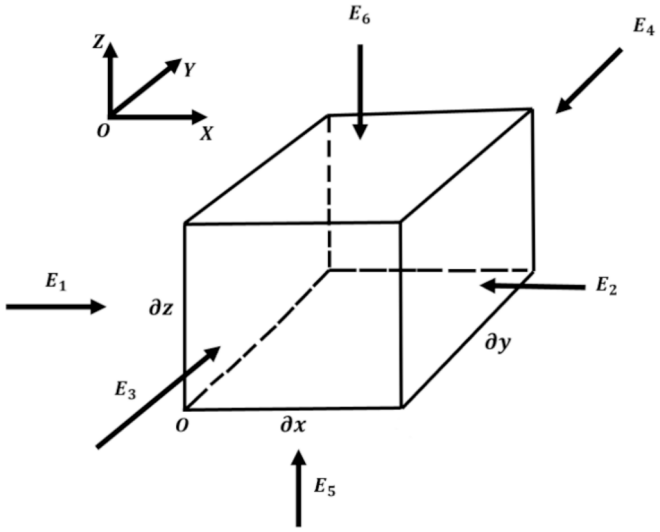

Fig. 1. Differential model for the radiant energy balance and assumptions of the SFM-2D. The incident light is normal to the z-y plane.

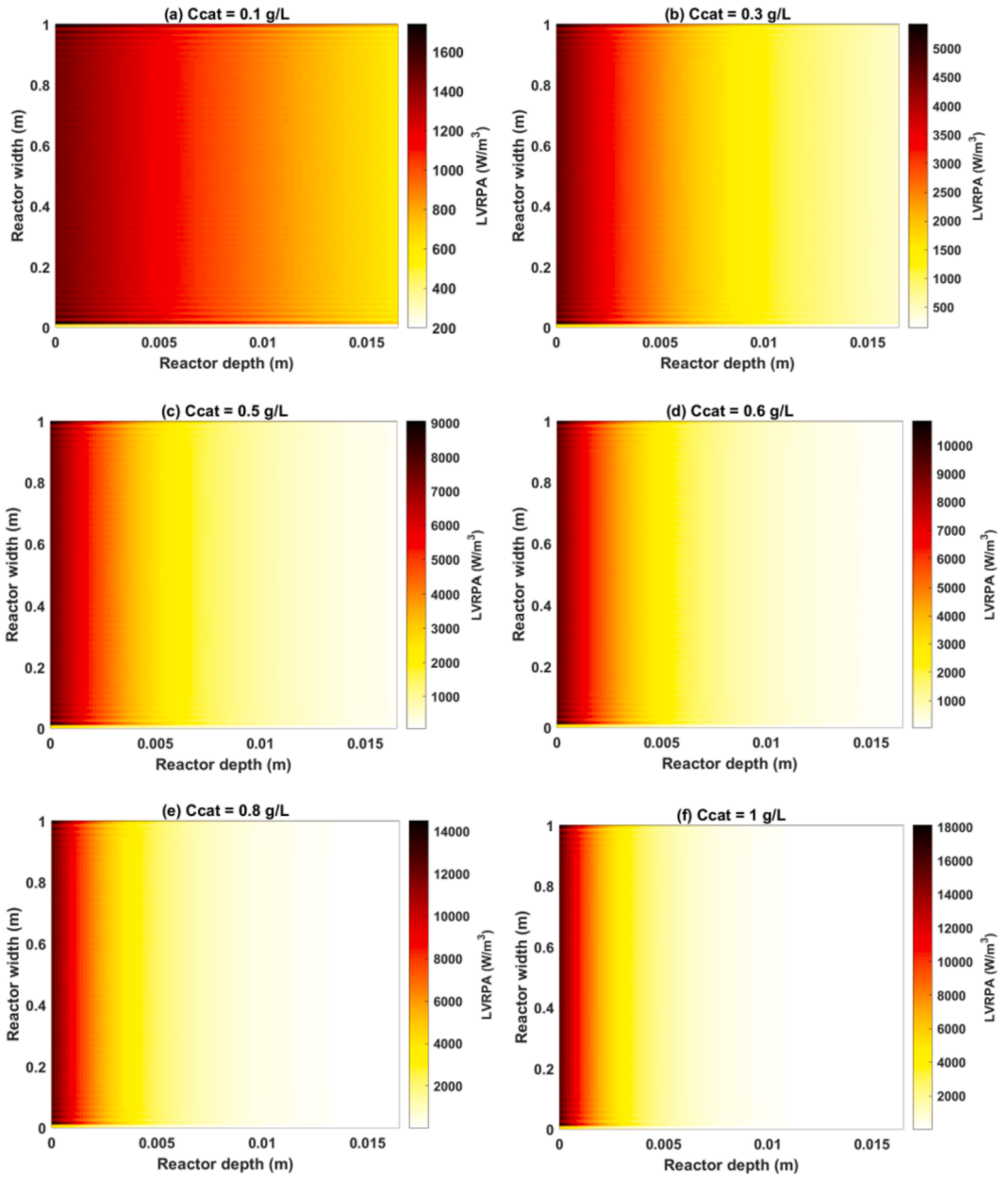

Fig. 2. Absorption profile in a slab reactor at different catalyst loadings ($L_p = 0.0165$ m, $L = 1$ m).

$$\frac{\partial(E_3)}{\partial y} = \frac{1}{\lambda_0}[(-1+\omega f)E_3 + \omega b E_4 + \omega s(E_1+E_2+E_5+E_6)] \quad (5)$$

$$\frac{\partial(E_4)}{\partial y} = \frac{1}{\lambda_0}[(+1-\omega f)E_4 - \omega b E_3 - \omega s(E_1+E_2+E_5+E_6)] \quad (6)$$

$$\frac{\partial(E_5)}{\partial z} = \frac{1}{\lambda_0}[(-1+\omega f)E_5 + \omega b E_6 + \omega s(E_1+E_2+E_3+E_4)] \quad (7)$$

$$\frac{\partial(E_6)}{\partial z} = \frac{1}{\lambda_0}[(+1-\omega f)E_6 - \omega b E_5 - \omega s(E_1+E_2+E_3+E_4)] \quad (8)$$

where ω is the scattering albedo of the suspended catalytic particle, λ_0 is the photon mean free path, and f, b, and s are the forward, backward, and sidewise-scattering probabilities, respectively, which match Eq. (9)

$$f + b + 4s = 1 \quad (9)$$

E_1, E_2, E_3, E_4, E_5 and E_6 represent the six discrete components of the specific radiation intensity (in this case E_1 is the incident beam, Fig. 1).f, b and s are calculated using a suitable phase function that describes the scattering behavior of the catalytic particles. The photon mean free path λ_0 within the differential control volume is related to the absorption and scattering of radiation by the suspended catalytic particles, and to the absorption of the water matrix and species in solution as follows:

$$\frac{1}{\lambda_0} = (\sigma^* + \kappa^*)c_{cat} + \sum_{i=1}^{n} \kappa_{ci}^* C_{ci} + \mu_w \quad (10)$$

where σ^*, κ^* are respectively the spectral-averaged catalyst specific mass absorption and scattering coefficients over the wavelength spectrum of the incident radiation [24], κ_{ci}^* is the spectral-averaged specific mass absorption coefficient of each dissolved reacting species in solution also over the wavelength spectrum of the incident radiation ; C_{ci} is the concentration of each reacting species (e.g, water contaminants) in the fluid, μ_w is the spectral-averaged background absorption of the water

matrix and c_{cat} is the catalyst loading. E_5 and E_6 are equal because of the symmetry consideration, since the photon flux is considered constant in the z direction.

The mathematical procedure and considerations used here to solve Eq. (3–9) follow Clovis Nchikou et al., (2021) [23] and are found in SI. This results in:

$$E_1 = \frac{1}{2}\sum_{K\le 0}\left[v_K\left(j_K\left(1-\frac{\sqrt{A\alpha_K}}{C_1+C_2}\right)e^{\sqrt{A\alpha_K}x} + l_K\left(1+\frac{\sqrt{A\alpha_K}}{C_1+C_2}\right)e^{-\sqrt{A\alpha_K}x}\right)\right] \tag{11}$$

$$E_2 = \frac{1}{2}\sum_{K\le 0}\left[v_K\left(j_K\left(1+\frac{\sqrt{A\alpha_K}}{C_1+C_2}\right)e^{\sqrt{A\alpha_K}x} + l_K\left(1-\frac{\sqrt{A\alpha_K}}{C_1+C_2}\right)e^{-\sqrt{A\alpha_K}x}\right)\right] \tag{12}$$

$$E_3 = \frac{\zeta}{2}\sum_{K\le 0}\left[u_K(1-\alpha_K)\left(\left(m_K-\frac{p_K\sqrt{-K}}{C_1+C_2}\right)cos\left(\sqrt{-K}y\right)+\left(p_K + \frac{m_K\sqrt{-K}}{C_1+C_2}\right)sin\left(\sqrt{-K}y\right)\right)\right] \tag{13}$$

$$E_4 = \frac{\zeta}{2}\sum_{K\le 0}\left[u_K(1-\alpha_K)\left(\left(m_K+\frac{p_K\sqrt{-K}}{C_1+C_2}\right)cos\left(\sqrt{-K}y\right)+\left(p_K - \frac{m_K\sqrt{-K}}{C_1+C_2}\right)sin\left(\sqrt{-K}y\right)\right)\right] \tag{14}$$

$$E_5 = E_6 = \frac{\omega s\sum_{K\le 0}\left[(1+\zeta(1-\alpha_K))\left(m_K cos\left(\sqrt{-K}y\right)+p_K sin\left(\sqrt{-K}y\right)\right)\left(j_K e^{\sqrt{A\alpha_K}x}+l_K e^{-\sqrt{A\alpha_K}x}\right)\right]}{(1-\omega f-\omega b)} \tag{15}$$

where, K, m_K, p_K, j_K, l_K are integration constants,

$$C_1 = \frac{1}{\lambda_0}\left(1-\omega f-\frac{2(\omega s)^2}{1-\omega f-\omega b}\right) \tag{16}$$

$$C_2 = \frac{1}{\lambda_0}\left(\omega b+\frac{2(\omega s)^2}{1-\omega f-\omega b}\right) \tag{17}$$

$$C_3 = \frac{1}{\lambda_0}\left(\omega s+\frac{2(\omega s)^2}{1-\omega f-\omega b}\right) \tag{18}$$

$$A = {C_1}^2 - {C_2}^2 \tag{19}$$

$$B = C_3(C_1+C_2) \tag{20}$$

$$C = A^2 - 4B^2 \tag{21}$$

$$\alpha_K = \frac{-K+\frac{C}{A}}{-K+A} \tag{22}$$

$$\zeta = \frac{A}{2B} \tag{23}$$

$$u_K = j_K e^{\sqrt{A\alpha_K}x} + l_K e^{-\sqrt{A\alpha_K}x} \tag{24}$$

$$v_K = m_K cos\left(\sqrt{-K}y\right) + p_K sin\left(\sqrt{-K}y\right) \tag{25}$$

The specific intensity of the radiation G is equal to $\sum_{i=1}^{6}E_i$ which leads to:

$$G(x,y) = \zeta^*\sum_{K\le 0}\left[(1+\zeta(1-\alpha_K))\left(m_K cos\left(\sqrt{-K}y\right)+p_K sin\left(\sqrt{-K}y\right)\right)\left(j_K e^{\sqrt{A\alpha_K}x}+l_K e^{-\sqrt{A\alpha_K}x}\right)\right] \tag{26}$$

where,

$$\zeta^* = 1+\frac{2\omega s}{(1-\omega f-\omega b)} \tag{27}$$

The integration constants are evaluated using suitable boundary conditions. The *LVRPA* can be obtained from a photon balance on the small volume comprised between $[x, x+\partial x]$, $[y, y+\partial y]$ and $[z, z+\partial z]$ [7] (Fig. 1 and SI),

$$LVRPA = \frac{\partial(E_2)}{\partial x}-\frac{\partial(E_1)}{\partial x}+\frac{\partial(E_4)}{\partial y}-\frac{\partial(E_3)}{\partial y}+\frac{\partial(E_6)}{\partial z}-\frac{\partial(E_5)}{\partial z} \tag{28}$$

Combining Eqs. (11–15) and (28) yields the *LVRPA*:

$$LVRPA = \sum_{K\le 0}\left[\frac{A\alpha_K+\zeta K(1-\alpha_K)}{C_1+C_2}\left(m_K cos\left(\sqrt{-K}y\right)+p_K sin\left(\sqrt{-K}y\right)\right)\left(j_K e^{\sqrt{A\alpha_K}x}+l_K e^{-\sqrt{A\alpha_K}x}\right)\right] \tag{29}$$

The volumetric rate of photon absorption per unit of the elementary volume height (*VRPA*) describes the absorption of photons inside each slide of the elementary volume parallel to the plane (x-y) (Fig. 3) since the symmetry is considered along the z-axis. It gives a broader view of the energy absorption and is calculated by integrating the *LVRPA* over the rectangle $[0, L_p]\times[0, L]$ as,

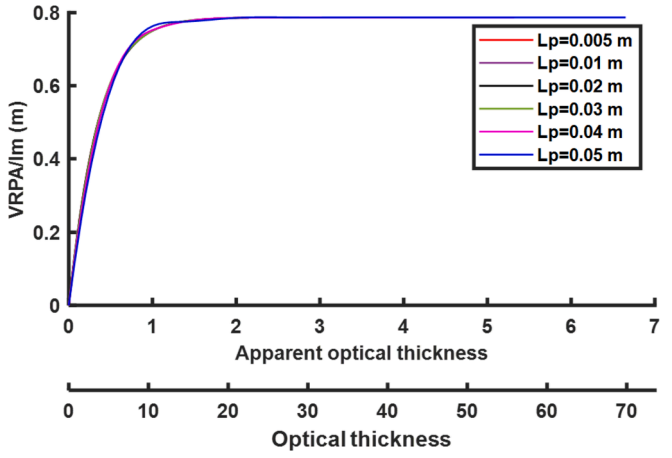

Fig. 3. The *VRPA*/I_m as a function of τ and τ_{App2} with different reactor depths L_p and with catalyst parameters in Table 1.

$$VRPA = \int_0^{L_p} \int_0^{L} LVRPA dx dy \tag{31}$$

where L_p and L are the depth and width of the rectangle (flat slab) along the x and y axes, respectively (Fig. S1, SI).

Considering that E_1 is the incident radiation flux to the slab, then, the transmitted and reflected photon fluxes at the front and back boundaries of the flat slab are defined respectively as follows:

$$\begin{aligned} T(y) &= E_1(L_p, y) \\ &= \frac{1}{2}\sum_{K\le 0}\left[\nu_K\left(j_K\left(1-\frac{\sqrt{A\alpha_K}}{C_1+C_2}\right)e^{\sqrt{A\alpha_K}L_p} \right.\right. \\ &\quad \left.\left. + l_K\left(1+\frac{\sqrt{A\alpha_K}}{C_1+C_2}\right)e^{-\sqrt{A\alpha_K}L_p}\right)\right] \end{aligned} \tag{33}$$

$$R(y) = E_2(0,y) = \frac{1}{2}\sum_{K\le 0}\left[\nu_K\left(j_K\left(1+\frac{\sqrt{A\alpha_K}}{C_1+C_2}\right)+l_K\left(1-\frac{\sqrt{A\alpha_K}}{C_1+C_2}\right)\right)\right] \tag{34}$$

2.2. Boundary conditions

The flat slab photocatalytic reactor shown in Fig. S1 may receive radiation at its front and rear with intensities q_f and q_r respectively. To obtain the integration constants that appear in Eq. (26), the boundary conditions in Eqs. (35–36) were applied at the reactor front ($x = 0$) and rear ($x = L_p$) walls respectively:

$$E_1(0,y) = \frac{1}{2}\sum_{K\le 0}\left[\nu_K\left(j_K\left(1-\frac{\sqrt{A\alpha_K}}{C_1+C_2}\right)+l_K\left(1+\frac{\sqrt{A\alpha_K}}{C_1+C_2}\right)\right)\right] = q_f \tag{35}$$

$$\begin{aligned} E_2(L_p,y) = \frac{1}{2}\sum_{K\le 0}\left[\nu_K\left(j_K\left(1+\frac{\sqrt{A\alpha_K}}{C_1+C_2}\right)e^{\sqrt{A\alpha_K}L_p}\right.\right. \\ \left.\left. + l_K\left(1-\frac{\sqrt{A\alpha_K}}{C_1+C_2}\right)e^{-\sqrt{A\alpha_K}L_p}\right)\right] = q_r \end{aligned} \tag{36}$$

In both cases, it was necessary to expand the total radiative flux entering through the reactor front q_f and rear q_r into a $2L$-Fourier series (in both cases q_r was supposed to be equal to zero) with respect to the y variable. The Fourier expansion of q_f and q_r is,

$$q_{f,r} = \frac{h_0}{2} + \sum_{n=1}^{+\infty}\left[h_n cos\left(\frac{n\pi}{L}y\right) + w_n sin\left(\frac{n\pi}{L}y\right)\right] \tag{37}$$

where h_n and w_n are $q_{f,r}$ (q_f or q_r) Fourier series expansion constants defined by Eq. (38–40) using the orthogonality relations between sine and cosine functions.

$$h_0 = \frac{1}{L}\int_{-L}^{L} q_{f,r}\,dy \tag{38}$$

$$h_n = \frac{1}{L}\int_{-L}^{L} q_{f,r} cos\left(\frac{n\pi}{L}y\right)dy \tag{39}$$

$$w_n = \frac{1}{L}\int_{-L}^{L} q_{f,r} sin\left(\frac{n\pi}{L}y\right)dy \tag{40}$$

Eqs. (35,37) impose that $\sqrt{-K}$ should be equal to $\frac{n\pi}{L}$, with n a positive integer. For simplicity, here we consider a slab irradiated only from one side ($q_r = 0$). Then combining Eqs. (35–40), the following relations can be obtained:

$$m_0\left(j_0\left(1-\frac{\sqrt{A\alpha_0}}{C_1+C_2}\right)+l_0\left(1+\frac{\sqrt{A\alpha_0}}{C_1+C_2}\right)\right) = \frac{1}{L}\int_{-L}^{L} q_f dy \tag{41}$$

$$\begin{aligned} m_0\left(j_0\left(1+\frac{\sqrt{A\alpha_0}}{C_1+C_2}\right)e^{\sqrt{A\alpha_0}L}+l_0\left(1-\frac{\sqrt{A\alpha_0}}{C_1+C_2}\right)e^{-\sqrt{A\alpha_0}L}\right) &= \frac{1}{L}\int_{-L}^{L} q_r dy \\ &= 0 \end{aligned} \tag{42}$$

$$m_n\left(j_n\left(1-\frac{\sqrt{A\alpha_n}}{C_1+C_2}\right)+l_K\left(1+\frac{\sqrt{A\alpha_n}}{C_1+C_2}\right)\right) = \frac{2}{L}\int_{-L}^{L} q_f cos\left(\frac{n\pi}{L}y\right)dy \tag{43}$$

$$m_n\left(j_n\left(1+\frac{\sqrt{A\alpha_n}}{C_1+C_2}\right)+l_K\left(1-\frac{\sqrt{A\alpha_n}}{C_1+C_2}\right)\right) = \frac{2}{L}\int_{-L}^{L} q_r cos\left(\frac{n\pi}{L}y\right)dy = 0 \tag{44}$$

$$p_n\left(j_n\left(1-\frac{\sqrt{A\alpha_n}}{C_1+C_2}\right)+l_K\left(1+\frac{\sqrt{A\alpha_n}}{C_1+C_2}\right)\right) = \frac{2}{L}\int_{-L}^{L} q_f sin\left(\frac{n\pi}{L}y\right)dy \tag{45}$$

$$p_n\left(j_n\left(1+\frac{\sqrt{A\alpha_n}}{C_1+C_2}\right)+l_K\left(1-\frac{\sqrt{A\alpha_n}}{C_1+C_2}\right)\right) = \frac{2}{L}\int_{-L}^{L} q_r sin\left(\frac{n\pi}{L}y\right)dy = 0 \tag{46}$$

Further, two circumstances with different boundary conditions were analyzed. The first case assumes that the incident radiation is collimated, perpendicular to the reactor front wall, and has constant intensity. The second case considers that the incident radiation varies along the y-axis while symmetry is maintained along the z-axis. The elementary volume in Fig. 1 was considered as an element of the flat slab reactor receiving the incident radiation E_1 at its front wall, i.e., at any point of the line (0, y).

2.2.1. Case 1: Incident radiation is collimated and perpendicular to the reactor front and constant

Let us suppose that the total solar radiative flux entering through the reactor front q_f and rear q_r are defined respectively as a periodic function with period $2L$ as follows:

$$q_f = \begin{cases} 0, if y \in [-L;0] - \{0\} \\ I_0, if y \in [0;L] \end{cases} \tag{47}$$

where I_0 is the incident radiation intensity reaching the reactor front boundary. Eqs. (37–40, 47) imply,

$$\frac{1}{L}\int_{-L}^{L} q_f dy = I_0 \tag{48}$$

$$\frac{2}{L}\int_{-L}^{L} q_f cos\left(\frac{n\pi}{L}y\right)dy = 0 \tag{49}$$

$$\frac{2\int_{-L}^{L} q_f sin\left(\frac{n\pi}{L}y\right)dy}{L} = \frac{2(1-(-1)^n)I_0}{n\pi} \tag{50}$$

Then, Eqs. (41–46, 48–50) turn to:

$$m_0\left(j_0\left(1-\frac{\sqrt{A\alpha_0}}{C_1+C_2}\right)+l_0\left(1+\frac{\sqrt{A\alpha_0}}{C_1+C_2}\right)\right) = I_0 \tag{51}$$

$$m_0\left(j_0\left(1+\frac{\sqrt{A\alpha_0}}{C_1+C_2}\right)e^{\sqrt{A\alpha_0}L}+l_0\left(1-\frac{\sqrt{A\alpha_0}}{C_1+C_2}\right)e^{-\sqrt{A\alpha_0}L}\right) = 0 \tag{52}$$

$$m_n\left(j_n\left(1-\frac{\sqrt{A\alpha_n}}{C_1+C_2}\right)+l_K\left(1+\frac{\sqrt{A\alpha_n}}{C_1+C_2}\right)\right) = 0 \tag{53}$$

$$m_n\left(j_n\left(1+\frac{\sqrt{A\alpha_n}}{C_1+C_2}\right)e^{\sqrt{A\alpha_n}L_p}+l_K\left(1-\frac{\sqrt{A\alpha_n}}{C_1+C_2}\right)e^{-\sqrt{A\alpha_n}L_p}\right) = 0 \tag{54}$$

$$p_n\left(j_n\left(1-\frac{\sqrt{A\alpha_n}}{C_1+C_2}\right)+l_K\left(1+\frac{\sqrt{A\alpha_n}}{C_1+C_2}\right)\right)=\frac{2(1-(-1)^n)I_0}{n\pi} \quad (55)$$

$$p_n\left(j_n\left(1+\frac{\sqrt{A\alpha_n}}{C_1+C_2}\right)e^{\sqrt{A\alpha_n}L_p}+l_K\left(1-\frac{\sqrt{A\alpha_n}}{C_1+C_2}\right)e^{-\sqrt{A\alpha_n}L_p}\right)=0 \quad (56)$$

Eq. (52) implies

$m_0=0$ or $j_0\left(1+\frac{\sqrt{A\alpha_0}}{C_1+C_2}\right)e^{\sqrt{A\alpha_0}L}+l_0\left(1-\frac{\sqrt{A\alpha_0}}{C_1+C_2}\right)e^{-\sqrt{A\alpha_0}L}=0$ but for Eq. (51) to make sense, m_0 should be different from zero. Then Eq. (52) leads to,

$$j_0\left(1+\frac{\sqrt{A\alpha_0}}{C_1+C_2}\right)e^{\sqrt{A\alpha_0}L}+l_0\left(1-\frac{\sqrt{A\alpha_0}}{C_1+C_2}\right)e^{-\sqrt{A\alpha_0}L}=0 \quad (57)$$

Eqs. (53,55) impose m_n to be equal to zero ($m_n=0$) and choosing for convenience the constant p_n equal to unity ($p_n=1$), Eqs. (51–52, 55–56) lead to solving simultaneously the following equations (taking $m_0=1$),

$$j_0\left(1-\frac{\sqrt{A\alpha_0}}{C_1+C_2}\right)+l_0\left(1+\frac{\sqrt{A\alpha_0}}{C_1+C_2}\right)=I_0 \quad (58)$$

$$j_0\left(1+\frac{\sqrt{A\alpha_0}}{C_1+C_2}\right)e^{\sqrt{A\alpha_0}L}+l_0\left(1-\frac{\sqrt{A\alpha_0}}{C_1+C_2}\right)e^{-\sqrt{A\alpha_0}L}=0 \quad (59)$$

For $n>0$ and n odd integer,

$$j_n\left(1-\frac{\sqrt{A\alpha_n}}{C_1+C_2}\right)+l_K\left(1+\frac{\sqrt{A\alpha_n}}{C_1+C_2}\right)=\frac{4I_0}{n\pi} \quad (60)$$

$$j_n\left(1+\frac{\sqrt{A\alpha_n}}{C_1+C_2}\right)e^{\sqrt{A\alpha_n}L_p}+l_n\left(1-\frac{\sqrt{A\alpha_n}}{C_1+C_2}\right)e^{-\sqrt{A\alpha_n}L_p}=0 \quad (61)$$

which leads to,

$$j_0=\frac{\left(1-\frac{\sqrt{A\alpha_0}}{C_1+C_2}\right)e^{-\sqrt{A\alpha_0}L_p}I_0}{\left(1-\frac{\sqrt{A\alpha_0}}{C_1+C_2}\right)^2e^{-\sqrt{A\alpha_0}L_p}-\left(1+\frac{\sqrt{A\alpha_0}}{C_1+C_2}\right)^2e^{\sqrt{A\alpha_0}L_p}} \quad (62)$$

$$l_0=\frac{-\left(1+\frac{\sqrt{A\alpha_0}}{C_1+C_2}\right)e^{\sqrt{A\alpha_0}L_p}I_0}{\left(1-\frac{\sqrt{A\alpha_0}}{C_1+C_2}\right)^2e^{-\sqrt{A\alpha_0}L_p}-\left(1+\frac{\sqrt{A\alpha_0}}{C_1+C_2}\right)^2e^{\sqrt{A\alpha_0}L_p}} \quad (63)$$

$$j_n=\frac{4\left(1-\frac{\sqrt{A\alpha_n}}{C_1+C_2}\right)e^{-\sqrt{A\alpha_n}L_p}I_0}{n\pi\left(\left(1-\frac{\sqrt{A\alpha_n}}{C_1+C_2}\right)^2e^{-\sqrt{A\alpha_n}L_p}-\left(1+\frac{\sqrt{A\alpha_n}}{C_1+C_2}\right)^2e^{\sqrt{A\alpha_n}L_p}\right)} \quad (64)$$

$$l_n=\frac{-4\left(1+\frac{\sqrt{A\alpha_n}}{C_1+C_2}\right)e^{\sqrt{A\alpha_n}L_p}I_0}{n\pi\left(\left(1-\frac{\sqrt{A\alpha_n}}{C_1+C_2}\right)^2e^{-\sqrt{A\alpha_n}L_p}-\left(1+\frac{\sqrt{A\alpha_n}}{C_1+C_2}\right)^2e^{\sqrt{A\alpha_n}L_p}\right)} \quad (65)$$

Combining Eqs. (62–65, 29), the *LVRPA* is deduced as,

$$LVRPA=\left(\frac{A\alpha_0}{C_1+C_2}\left(j_0e^{\sqrt{A\alpha_0}x}+l_0e^{-\sqrt{A\alpha_0}x}\right)+\sum\nolimits_{n=1,n\ odd\ integer}^{+\infty}\left(\frac{A\alpha_n+\zeta n(1-\alpha_n)}{C_1+C_2}sin\left(\frac{n\pi}{L}y\right)\left(j_ne^{\sqrt{A\alpha_n}x}+l_ne^{-\sqrt{A\alpha_n}x}\right)\right)\right) \quad (66)$$

and the *VRPA* over the entire slab is:

$$VRPA=\int_0^{L_p}\int_0^{L}\left(\frac{A\alpha_0}{C_1+C_2}\left(j_0e^{\sqrt{A\alpha_0}x}+l_0e^{-\sqrt{A\alpha_0}x}+\sum\nolimits_{n=1,n\ odd\ integer}^{+\infty}\left[\frac{A\alpha_n+\zeta n(1-\alpha_n)}{C_1+C_2}sin\left(\frac{n\pi}{L}y\right)\left(j_ne^{\sqrt{A\alpha_n}x}+l_ne^{-\sqrt{A\alpha_n}x}\right)\right]\right)\right)dxdy \quad (67)$$

which gives,

$$VRPA=\frac{\sqrt{A\alpha_0}L\left(j_0\left(e^{\sqrt{A\alpha_0}L_p}-1\right)-l_0\left(e^{-\sqrt{A\alpha_0}L_p}-1\right)\right)}{C_1+C_2}+2\sum\nolimits_{n=1,n\ odd\ integer}^{+\infty}\left[\frac{L(A\alpha_n+\zeta n(1-\alpha_n))\left(j_n\left(e^{\sqrt{A\alpha_n}L_p}-1\right)-l_n\left(e^{-\sqrt{A\alpha_n}L_p}-1\right)\right)}{n\pi\sqrt{A\alpha_n}(C_1+C_2)}\right] \quad (68)$$

2.2.2. Case 2: Incident radiation is collimated and perpendicular to the reactor front and varies along the reactor width (the y-variable)

As stated in the first case, the total radiative flux entering through the reactor front q_f and rear q_r are defined respectively as a 2*L*-periodic functions. Let us consider that the reactor is illuminated by a long cylindrical lamp with the radiation emission modeled as follows,

$$q_f=\begin{cases}0, if y\in[-L;0]-\{0\}\\ e^{\frac{-y}{L}}I_m, if y\in[0;L]\end{cases} \quad (69)$$

where I_m represents the irradiance measured at the lamp wall. Then Eqs. (37–40, 69) lead to

$$\frac{1}{L}\int_{-L}^{L}q_fdy=\left(1-\frac{1}{e}\right)I_m \quad (70)$$

$$\frac{1}{L}\int_{-L}^{L}q_fcos\left(\frac{n\pi}{L}y\right)dy=\begin{cases}\frac{1}{1+(n\pi)^2}\left(1+\frac{1}{e}\right)I_m;\ if\ n\ is\ an\ odd\ number\\ 0;\ if\ n\ is\ an\ even\ number\end{cases} \quad (71)$$

$$\frac{1}{L}\int_{-L}^{L}q_fsin\left(\frac{n\pi}{L}y\right)dy=\begin{cases}\frac{n\pi}{1+(n\pi)^2}\left(1+\frac{1}{e}\right)I_m;\ if\ n\ is\ an\ odd\ number\\ 0;\ if\ n\ is\ an\ even\ number\end{cases} \quad (72)$$

Eqs. (41–46, 70–72) turn to

$$m_0\left(j_0\left(1-\frac{\sqrt{A\alpha_0}}{C_1+C_2}\right)+l_0\left(1+\frac{\sqrt{A\alpha_0}}{C_1+C_2}\right)\right)=\left(1-\frac{1}{e}\right)I_m \quad (73)$$

$$m_0\left(j_0\left(1+\frac{\sqrt{A\alpha_0}}{C_1+C_2}\right)+l_0\left(1-\frac{\sqrt{A\alpha_0}}{C_1+C_2}\right)\right)=0 \tag{74}$$

If n is an odd number,

$$m_n\left(j_n\left(1-\frac{\sqrt{A\alpha_n}}{C_1+C_2}\right)+l_K\left(1+\frac{\sqrt{A\alpha_n}}{C_1+C_2}\right)\right)=\frac{2}{1+(n\pi)^2}\left(1+\frac{1}{e}\right)I_m \tag{75}$$

$$m_n\left(j_n\left(1+\frac{\sqrt{A\alpha_n}}{C_1+C_2}\right)+l_K\left(1-\frac{\sqrt{A\alpha_n}}{C_1+C_2}\right)\right)=0 \tag{76}$$

$$p_n\left(j_n\left(1-\frac{\sqrt{A\alpha_n}}{C_1+C_2}\right)+l_K\left(1+\frac{\sqrt{A\alpha_n}}{C_1+C_2}\right)\right)=\frac{2n\pi}{1+(n\pi)^2}\left(1+\frac{1}{e}\right)I_m \tag{77}$$

$$p_n\left(j_n\left(1+\frac{\sqrt{A\alpha_n}}{C_1+C_2}\right)e^{\sqrt{A\alpha_n}L_p}+l_K\left(1-\frac{\sqrt{A\alpha_n}}{C_1+C_2}\right)e^{-\sqrt{A\alpha_n}L_p}\right)=0 \tag{78}$$

Taking $m_n = 1$, $p_n = n\pi$ and $m_0 = 1$ leads to solving simultaneously the following equations,

$$j_0\left(1-\frac{\sqrt{A\alpha_0}}{C_1+C_2}\right)+l_0\left(1+\frac{\sqrt{A\alpha_0}}{C_1+C_2}\right)=\left(1-\frac{1}{e}\right)I_m \tag{79}$$

$$j_0\left(1+\frac{\sqrt{A\alpha_0}}{C_1+C_2}\right)e^{\sqrt{A\alpha_0}L}+l_0\left(1-\frac{\sqrt{A\alpha_0}}{C_1+C_2}\right)e^{-\sqrt{A\alpha_0}L}=0 \tag{80}$$

For $n > 0$ and n odd integer,

$$j_n\left(1-\frac{\sqrt{A\alpha_n}}{C_1+C_2}\right)e^{\sqrt{A\alpha_n}L_p}+l_n\left(1+\frac{\sqrt{A\alpha_n}}{C_1+C_2}\right)e^{-\sqrt{A\alpha_n}L_p}=\frac{2}{1+(n\pi)^2}\left(1+\frac{1}{e}\right)I_m \tag{81}$$

$$2\sum_{n=1,\ with\ n\ odd\ integer}^{+\infty}\left[\frac{L(A\alpha_n+\zeta n(1-\alpha_n))\left(j_n\left(e^{\sqrt{A\alpha_n}L_p}-1\right)-l_n\left(e^{-\sqrt{A\alpha_n}L_p}-1\right)\right)}{\sqrt{A\alpha_n}\,(C_1+C_2)}\right] \tag{89}$$

$$j_n\left(1+\frac{\sqrt{A\alpha_n}}{C_1+C_2}\right)+l_n\left(1-\frac{\sqrt{A\alpha_n}}{C_1+C_2}\right)=0 \tag{82}$$

which leads to,

$$j_0=\frac{\left(1-\frac{\sqrt{A\alpha_0}}{C_1+C_2}\right)e^{-\sqrt{A\alpha_0}L_p}\left(1-\frac{1}{e}\right)I_m}{\left(1-\frac{\sqrt{A\alpha_0}}{C_1+C_2}\right)^2e^{-\sqrt{A\alpha_0}L_p}-\left(1+\frac{\sqrt{A\alpha_0}}{C_1+C_2}\right)^2e^{\sqrt{A\alpha_0}L_p}} \tag{83}$$

$$l_0=\frac{-\left(1+\frac{\sqrt{A\alpha_0}}{C_1+C_2}\right)e^{\sqrt{A\alpha_0}L_p}\left(1-\frac{1}{e}\right)I_m}{\left(1-\frac{\sqrt{A\alpha_0}}{C_1+C_2}\right)^2e^{-\sqrt{A\alpha_0}L_p}-\left(1+\frac{\sqrt{A\alpha_0}}{C_1+C_2}\right)^2e^{\sqrt{A\alpha_0}L_p}} \tag{84}$$

$$j_n=\frac{2\left(1-\frac{\sqrt{A\alpha_n}}{C_1+C_2}\right)e^{-\sqrt{A\alpha_n}L_p}\left(1+\frac{1}{e}\right)I_m}{\left(1+(n\pi)^2\right)\left(\left(1-\frac{\sqrt{A\alpha_n}}{C_1+C_2}\right)^2e^{-\sqrt{A\alpha_n}L_p}-\left(1+\frac{\sqrt{A\alpha_n}}{C_1+C_2}\right)^2e^{\sqrt{A\alpha_n}L_p}\right)} \tag{85}$$

$$l_n=\frac{-2\left(1+\frac{\sqrt{A\alpha_n}}{C_1+C_2}\right)e^{\sqrt{A\alpha_n}L_p}\left(1+\frac{1}{e}\right)I_m}{\left(1+(n\pi)^2\right)\left(\left(1-\frac{\sqrt{A\alpha_n}}{C_1+C_2}\right)^2e^{-\sqrt{A\alpha_n}L_p}-\left(1+\frac{\sqrt{A\alpha_n}}{C_1+C_2}\right)^2e^{\sqrt{A\alpha_n}L_p}\right)} \tag{86}$$

Combining Eqs. (83–86, 29), the *LVRPA* is deduced as,

$$LVRPA=\left(\frac{A\alpha_0}{C_1+C_2}\left(j_0e^{\sqrt{A\alpha_0}x}+l_0e^{-\sqrt{A\alpha_0}x}\right)+\sum_{n=1,\ with\ n\ odd\ integer}^{+\infty}\left(\frac{A\alpha_n+\zeta n(1-\alpha_n)}{C_1+C_2}\left(cos\left(\frac{n\pi}{L}y\right)+n\pi sin\left(\frac{n\pi}{L}y\right)\right)\left(j_ne^{\sqrt{A\alpha_n}x}+l_ne^{-\sqrt{A\alpha_n}x}\right)\right)\right) \tag{87}$$

and the *VRPA* as,

$$VRPA=\int_0^{L_p}\int_0^{L}\left(\frac{A\alpha_0}{C_1+C_2}\left(j_0e^{\sqrt{A\alpha_0}x}+l_0e^{-\sqrt{A\alpha_0}x}\right)+\sum_{n=1,\ with\ n\ odd\ integer}^{+\infty}\left[\frac{A\alpha_n+\zeta n(1-\alpha_n)}{C_1+C_2}\left(cos\left(\frac{n\pi}{L}y\right)+n\pi sin\left(\frac{n\pi}{L}y\right)\right)\left(j_ne^{\sqrt{A\alpha_n}x}+l_ne^{-\sqrt{A\alpha_n}x}\right)\right]\right)dxdy \tag{88}$$

Or

$$VRPA=\frac{\sqrt{A\alpha_0}L\left(j_0\left(e^{\sqrt{A\alpha_0}L_p}-1\right)-l_0\left(e^{-\sqrt{A\alpha_0}L_p}-1\right)\right)}{C_1+C_2}+$$

2.2.3. Optimization of absorption radiation in slab reactors of any reactor depth

The reactor "optical thickness" τ and the "SFM-2D apparent optical thickness" τ_{app2} are dimensionless parameters introduced to optimize the radiation absorption in slab reactors of any depth. It is worth mentioning that τ is well known in literature and is defined by Eq. (90) using Eq. (10), while τ_{app2} (Eq. (91)) is a new optimization parameter that is associated with the SFM-2D approach.

$$\tau=\frac{L_p}{\lambda_0} \tag{90}$$

$$\tau_{app2}=\tau\lambda_0^2A\sqrt{1-\omega_{Corr2}^2} \tag{91}$$

where ω_{corr2} defined in Eq. (92) stands for the corrected catalyst albedo formulated with the SFM-2D approach:

$$\omega_{corr2}=\frac{1}{\zeta} \tag{92}$$

Table. 1
Flat slab reactor parameters used for the model simulation.

Reactor width	$L = 1\ m$
Reactor depth (L_p)	L_p(m) varying
Catalyst (TiO_2) of wavelength between 295–384 nm	Evonik P-25 Aeroxide [25]
The catalyst loading: C_{cat} (g/L)	Starting from zero g/L
The specific mass absorption coefficient κ^* (m^2/kg)	174.75 [25]
The specific mass scattering coefficient σ^*(m^2/kg)	1295.75 [25]
The scattering albedo $\omega = \frac{\sigma}{\sigma+\kappa+\kappa_c}$	0.88
The specific mass absorption of a given dissolved water contaminant: κ_c (m^{-1}) (see Eq. (10))	Considered here equal to zero
Phase function	Henyey-Greenstein phase function ($g = 0.53$) [20]
Scattering probabilities	$f = 0.754, b = 0.133\ s = 0.028$ [20]
Solar incident radiation intensity	$I_0 = 30\ W/m^2$
Irradiance measured at the reactor front wall	$I_m = 30\ W/m^2$

Using the one-dimensional SFM (SFM-1D) on a compound parabolic collector (CPC), it has been shown that τ removes the dependence of the optimum catalyst loading on the reactor depth [13]. In this study, it is shown that τ_{app2} not only removes the dependence of optimum catalyst loading on reactor depth, likewise τ does, but also on catalyst scattering albedo ω, similarly, the parameter τ_{app} (Eq. (83) in SI) derived from the SFM-1D [13]. The definitions and derivations used to obtain Eqs. (91–92) are similar to those in the SFM-1D model, representing an extension from 1D to 2D. The parameter ζ is the inverse of the corrected albedo ω_{corr2}, as shown in Eq. (92); therefore, ζ and ω_{corr2} vary inversely; ω_{corr2} is a corrected form of the conventional scattering albedo (ω) that accounts for the influence of the scattering phase function (see Eqs. (14–16, 33–34, 63, SI). When the phase function is dominated by backward scattering, ω_{corr2} is high (ζ is low), resulting in a higher ω. Conversely, when forward scattering is predominant, ω_{corr2} is low (ζ is high), leading to a lower ω. Backward scattering reduces the likelihood of photon absorption, whereas forward scattering enhances it by allowing photons to penétrate deeper into the reactor.

2.3. Model simulation conditions

Simulations were made on a flat slab reactor with different features as shown in Table 1. The catalyst optical properties were those of TiO_2-P25, and the values reported are those averaged over the solar radiation spectrum [25]. The absorption of the water matrix and the dissolved species in solution was assumed to be negligible in comparison to the absorption of light by the catalyst in suspension, over the spectrum of the incident radiation. Such an assumption is often verified in many photocatalytic systems for water detoxification, however, the model as presented can also include the absorption of the fluid matrix and all reactive species in solution (Eq. (10)). The integrated model was implemented and executed using MATLAB R2024b (MathWorks, USA). Simulations were performed on a Microsoft Surface Pro 8 with an 11th Gen Intel Core i5-1145G7 processor (2.60 GHz, 16 GB RAM) running Windows 11.

3. Results and discussion

3.1. First boundary case: Flat plate reactor with constant incident radiation

3.1.1. Photon absorption distribution

Fig. 2 displays the radiation absorption distribution inside the reactor ($L_p = 0.0165$ m, $L = 1$ m) at catalyst concentrations from 0.1 to 1.0 g/L. The light absorption remains invariant along the reactor width since in this case the incident radiation is constant along the reactor width, thus for constant x, the *LVRPA* along the y-axis remains constant. Thus, the model simulations show that as the catalyst concentration increases from 0.1 to 1.0 g/L, the *LVRPA* progressively increases near the front wall and decreases near its back wall, and at catalyst loadings higher than 0.6 g/L, an increasing fraction of the reactor near the back wall remains practically under dark conditions. Thus, at high values of the optical thickness, depending on the value of the catalyst scattering albedo, the reactor begins to work under non-optimal settings. In contrast, the absorption profile shows a more gradual distribution of the radiant energy in the reactor at catalyst loadings lower than approximately 0.6 g/L. It is also clear that as the catalyst concentration is progressively increased, the total amount of energy absorbed in the reactor continues to increase, but this energy is not spatially well distributed along the entire reactor depth [23]; thus, negligible photocatalytic reactions occur in the dark region of the slab. Often, these observations have been described in literature in a qualitative way as a *clouding effect* by the suspended particles, preventing light from reaching the inner regions of the reactor. These conditions are, however, not unique to the catalyst used but instead are dependent on the reactor depth, meaning that reactors with smaller depth should be operated at higher catalyst concentrations, while reactors with greater depth should be operated at smaller catalyst concentrations. Often, this important aspect is overlooked in many kinetic studies reported in the wider literature, thus, the kinetics of different catalyst specimens are compared in the same reactor geometry and at the same catalyst concentration (often chosen arbitrarily as 1.0 g/L). To resolve these uncertainties, some meaningful dimensionless parameters should be used to determine the most suitable catalyst loading in a specific photoreactor. As already mentioned, these are the optical thicknesses τ and τ_{App2} (Eqs. 90–92), which can be used interchangeably for reactor optimization. The optical thicknesses τ remove the dependence of the optimum catalyst loading on reactor depth L_p (or reactor diameter in CPC reactors [13]) but vary with catalyst albedo, while the apparent optical thickness τ_{App2} also removes the dependence on catalyst albedo ω. For the reaction conditions, the values of τ and τ_{App2} corresponding to a catalyst loading of 0.6 g/L are

Table. 3
The optimum values of C_{cat} ($C_{cat,op}$), τ (τ_{op}), τ_{app} ($\tau_{app,op}$) and τ_{App2} ($\tau_{App2,op}$) with different catalyst albedo ($\kappa^* = 174.75\ m^2/kg$). τ_{app} stands for the apparent thickness calculated with the SFM-1D approach.

ω	$C_{cat,op}$	τ_{op}	$\tau_{App2,op}$	$\tau_{app,op}$
0.75	1.16	8.44	1.47	4.79
0.8	0.92	10.48	1.47	4.79
0.85	0.69	13.54	1.47	4.79
0.88	0.67	16.26	1.47	4.79

Table 2
Optimum catalyst loading ($C_{cat,op}$), apparent optical thickness with the SFM-2D and the SFM-1D ($\tau_{App2,op}$, $\tau_{app,op}$), and optical thickness (τ_{op}) for different reactor depths. The reactor operating conditions are from Table 1.

L_p(cm)	0.5	1	2	3	4	5	6	7	8
$C_{cat,op}$(g/L)	2.208	1.104	0.552	0.368	0.276	0.221	0.184	0.158	0.138
$\tau_{App2,op}$	1.47	1.47	1.47	1.47	1.47	1.47	1.47	1.47	1.47
$\tau_{app,op}$	4.79	4.79	4.79	4.79	4.79	4.79	4.79	4.79	4.79
τ_{op}	16.3	16.3	16.3	16.3	16.3	16.3	16.3	16.3	16.3

equal to 14.56 and 1.32, respectively.

3.1.2. Optimum values of τ and τ_{App2}

As stated in the previous section, the reactor optical thickness τ removes the dependence of the optimum catalyst loading on the reactor depth L_p, while τ_{app2} removes the dependence of optimum catalyst loading on both reactor depth and catalyst scattering albedo ω. To prove these two points, firstly, the *VRPA* per unit of the irradiance measured at the reactor front wall ($VRPA/I_m$) was evaluated as a function of τ and τ_{App2} with different reactor depths as shown in Fig. 3; then the optimum values of both τ and τ_{App2} were estimated keeping the reactor depth and the catalyst specific absorption coefficient constant while varying the catalyst scattering albedo (Table 3).

Fig. 3 shows that $VRPA/I_m$ increases with τ and τ_{App2} until a plateau is reached and that the results remain invariant when varying the reactor depth, which proves the independency of these dimensionless parameters on the reactor depth. Thus, optimum values of both τ and τ_{App2} can be determined in the region approaching the plateau.

Table 2 shows the optimum catalyst loading and the corresponding optimum apparent optical thickness and optical thickness that yields 99 % of the ($VRPA/I_m$) at different reactor depths. The optimum catalyst loading for any reactor depth led to the same amount of radiation absorption ($VRPA/I_m = 0.78$ m) and almost the same value of optical thickness and apparent optical thicknesses with the discrepancies due to the precision of the numerical method. The optimum apparent optical thickness for the SFM-1D ($\tau_{app,op}$) was more than three times that found with the SFM-2D ($\tau_{app2,op}$), as shown in Table 2.

On the other hand, when varying catalyst albedo while keeping κ^* constant, τ_{op} varied considerably, while $\tau_{App2,op}$ and $\tau_{app,op}$ remained constant as shown in Table 3.

In conclusion, the optimum optical thickness τ_{op} depends on catalyst albedo while $\tau_{App2,op}$ does not, therefore, τ_{App2} provides a more generalized reactor optimization parameter than τ. The major practical implication of these findings is that when assessing the activity of different photocatalyst specimens in suspension using the same photoreactor, the optimum catalyst concentration is likely to differ among such specimens, unless such catalysts have the same scattering albedo ω. This situation is very unlikely to happen since catalyst surface morphology, surface charge, and catalyst particle agglomeration have a profound effect on the value of the scattering albedo of the catalyst suspensions. Thus, many conclusions in the wider literature on "best catalysts" may need to be revisited.

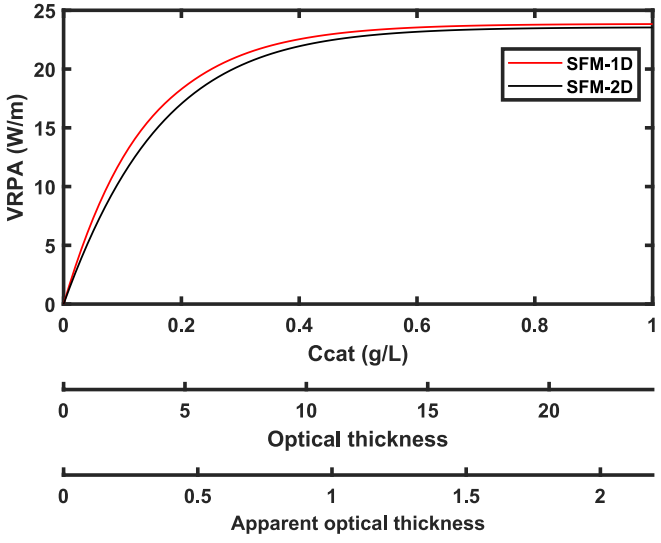

Fig. 4. The *VRPA* vs catalyst loading, apparent optical thickness, and optical thickness with the SFM-1D (red line) and the SFM-2D (black line) ($L_p = 0.0165$ m, $L = 1$ m).

The results in Table 2 show that the optimum photon absorption for the TiO_2-P25 photocatalyst occurs at an apparent optical thickness, $\tau_{App2,op}$, of 1.47 in slab photocatalytic reactors. This corresponds to an optical thickness, τ, of 16.3, which is somewhat different from the value of 11.41 reported in the literature, where the SFM-1D model and diffuse reflectance (DR) phase function were used but with catalyst properties differing from those in this work [26]. Maintaining $\tau_{App2,op}$ constant yields the optimal design conditions for different catalyst loadings and reactor thicknesses, and slab photocatalytic reactors working at the same $\tau_{App2,op}$ keep the same radiation absorption behavior.

3.1.3. Comparison of the VRPA using the SFM1-D and the SFM2-D

The *VRPA* calculated using the SFM-1D (see SI) and SFM-2D was obtained by integrating the *LVRPA* over the rectangle of width L and depth L_p.

Fig. 4 shows the *VRPA* as a function of catalyst loading, optical thickness, and apparent optical thickness, calculated using the SFM-1D (red line) and the SFM-2D (black line). Both models show the same behavior, increasing exponentially and approaching a plateau at approximately 0.6 g/L of catalyst loading. The same behavior was found by Brandi et al., (1996) [27] and Otálvaro et al., (2014) [26] in a flat plate photoreactor, and Clovis Nchikou et al., (2021) [23] in a CPC photoreactor. The *VRPA* with the SFM-2D is slightly below the *VRPA* with the SFM-1D, with an overall discrepancy of about 17.6 % using the root mean square percentage in the catalyst loading between 0 and 1 g/L. This disparity occurs since the SFM-1D assumes two symmetry considerations while the SFM-2D assumes only one. Assuming many symmetry considerations in the SFM-1D leads to excessive simplification of the RTE and therefore increases discrepancies with the exact solution of the RTE and to an overestimation of the radiation absorption.

3.1.4. Impact of the catalyst optical parameters and scattering phase function on radiation absorption

The *LVRPA* and *VRPA* in the slab were calculated with the SFM-2D using the H-G and the DR scattering phase functions to evaluate their impact on radiation absorption (Figs. 5-6).

The distribution of radiation absorption across the slab is clearly more uniform with the H-G scattering phase function since it favors forward scattering over the predominantly backward scattering of the DR phase function. Thus, with the H-G scattering phase function, photons can more easily reach the inner part of the reactor in comparison to the DR phase function. On the other hand, with the DR phase function, the back scattering is very high at the zone near the front reactor wall, thus, higher absorption was observed near this region in comparison to the H-G phase function. The same observations were made when using a CPC reactor [23]. Further, the *VRPA* calculated with both phase functions, exhibited a similar trend as shown in Fig. 6, but the absorption plateau observed with the H-G was higher than with the DR. This is clearly shown in Fig. 6 that display the $VRPA/I_m$ as a function of C_{cat} calculated using using the H-G (plateau at 0.67 m) and DR (plateau at 0.42 m) phase functions (black lines) but with catalyst optical parameters ($\kappa^* = 287$ (m^2/kg), $\sigma^* = 5420$ (m^2/kg), and $\omega = 0.95$) taken from literature [26]. The H-G scattering phase function is recognised as a better description of the scattering properties of TiO_2 particles in aqueous suspensions [20] when compared to the DR phase function.

3.2. Second boundary case: Flat plate reactor with incident radiation varying along the y-coordinate

3.2.1. Radiation absorption behavior

The second case considers that the incident radiation varies along the y-axis with an exponential decay (Eq. (69) while symmetry is maintained along the z-axis. Fig. 7 shows the radiation absorption distribution inside the reactor ($L_p = 0.0165$ m, $L = 1$ m) at catalyst

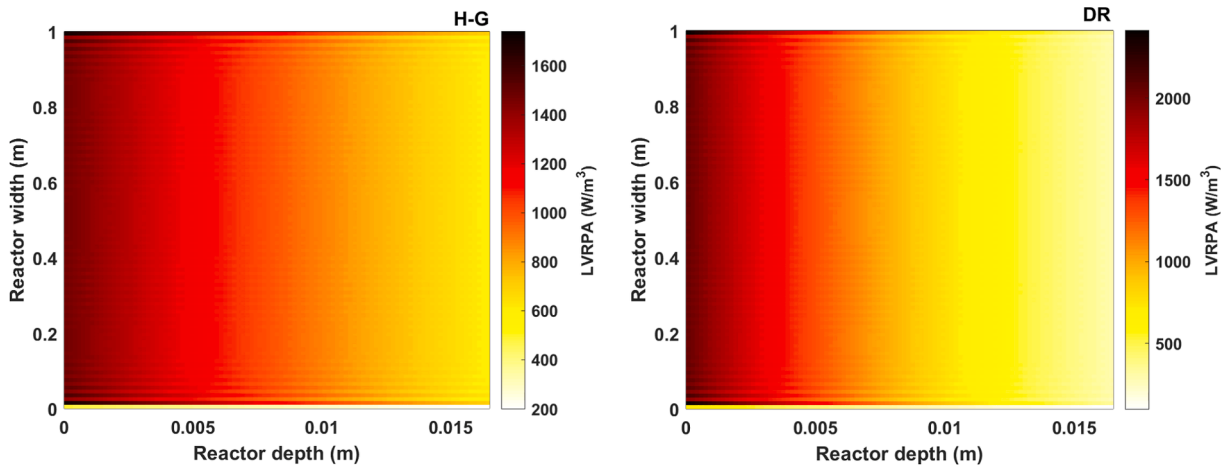

Fig. 5. The *LVRPA* profile in the slab withL_p = 0.0165 m, C_{cat}= 0.1 g/L. Catalyst parameters from Table 1 and H-G phase function (left). Catalyst parameters from Table 1 but H-G phase function replaced with DR phase function with scattering probabilities: forward f = 0.11; backward b = 0.71; side s = 0.045 (right) [12].

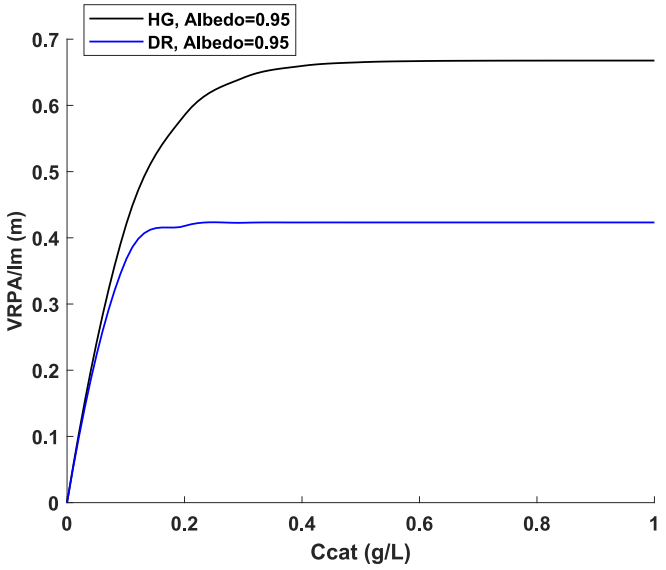

Fig. 6. The *VRPA* per unit of the irradiance measured at the reactor front wall as a function of C_{cat} with different catalyst parameters, straight black and blue lines stand for the *VRPA*/Im calculated with H-G and DR phase functions, respectively, and both with $\kappa^* = 287$ (m^2/kg), $\sigma^* = 5420$ (m^2/kg), and ω = 0.95.

concentrations from 0.1 to 1.0 g/L. The *LVRPA* now varies along the reactor width since the incident radiation decreases exponentially along the reactor width from 0 to L (see Fig. S2, SI) and also varies along the reactor depth. The *LVRPA* is clearly not uniform across the x-y plane. As the catalyst concentration is increased, the distribution of radiation becomes less uniform across the reactor, with sharper gradients near the front wall of the reactor. Moreover, at catalyst concentrations approximately higher than 0.5 g/L, the radiation absorption decreases notably due to the particles' clouding effect, which impedes the photons' penetration to the inner part of the reactor. The result in this figure shows the predictive capability of the SFM-2D, while the SFM-1D would have been unsuitable due to the failure of its assumption on uniform irradiation at the front wall. The *VRPA* also increases with catalyst loading, optical thickness, and apparent optical thickness until a plateau is approximated at catalyst concentrations higher than 0.6 g/L (Fig. 8). The same recommendation made in the first boundary case should be followed here for optimization purposes. The optimum values of τ_{op} and $\tau_{App2,op}$ are almost the same as in the first boundary case, where the incident radiation intensity was constant. It is also observed in this case that the light absorption decreases exponentially along the reactor width since in this case the incident radiation varies along the reactor width, thus, for every value of x, the *LVRPA* decreases exponentially with respect to y.

3.2.2. Independence of optimum values of τ (τ_{op}) and τ_{App2}($\tau_{App2,op}$) on reactor depth and catalyst albedo

As previously shown for the boundary condition (1), the independence of both τ_{op} and $\tau_{App2,op}$ on the reactor depth and the independence of $\tau_{App2,op}$ on the catalyst albedo was proved by evaluating firstly the *VRPA*/Im as a function of τ and τ_{App2} at different reactor depths (see Fig. 9); then τ_{op} and $\tau_{App2,op}$ were estimated keeping the reactor depth and the catalyst specific absorption coefficient constant, while varying the catalyst scattering albedo ω.

Fig. 9 shows that the *VRPA*/Im remains the same with respect to τ and τ_{App2} when varying the reactor depth; thus τ_{op} and $\tau_{App2,op}$ are the same no matter the change of L_p which proves the independence of these dimensionless parameters on the reactor depth. As in the first case, when varying catalyst albedo and keeping κ^* constant, τ_{op} varied considerably as expected, while $\tau_{App2,op}$ remained effectively constant. The values of τ_{op} and $\tau_{App2,op}$ determined in this case were similar to those found in the first case (Table 2 and Table 3), which also proves that these parameters do not vary with the intensity of the incident radiation at the reactor boundary.

3.2.3. Impact of the reactor depth on theVRPA

Fig. 10 illustrates how the *VRPA* varies with reactor depth for different catalyst loading (0.1–0.5 g/L). The higher the catalyst loading, the lower the optimum reactor depth that leads to the maximum value of radiation absorption in the slab.

For any catalyst loading, the *VRPA* increases exponentially with the reactor depth until reaching a fixed value ($VRPA_{op}$) beyond which no

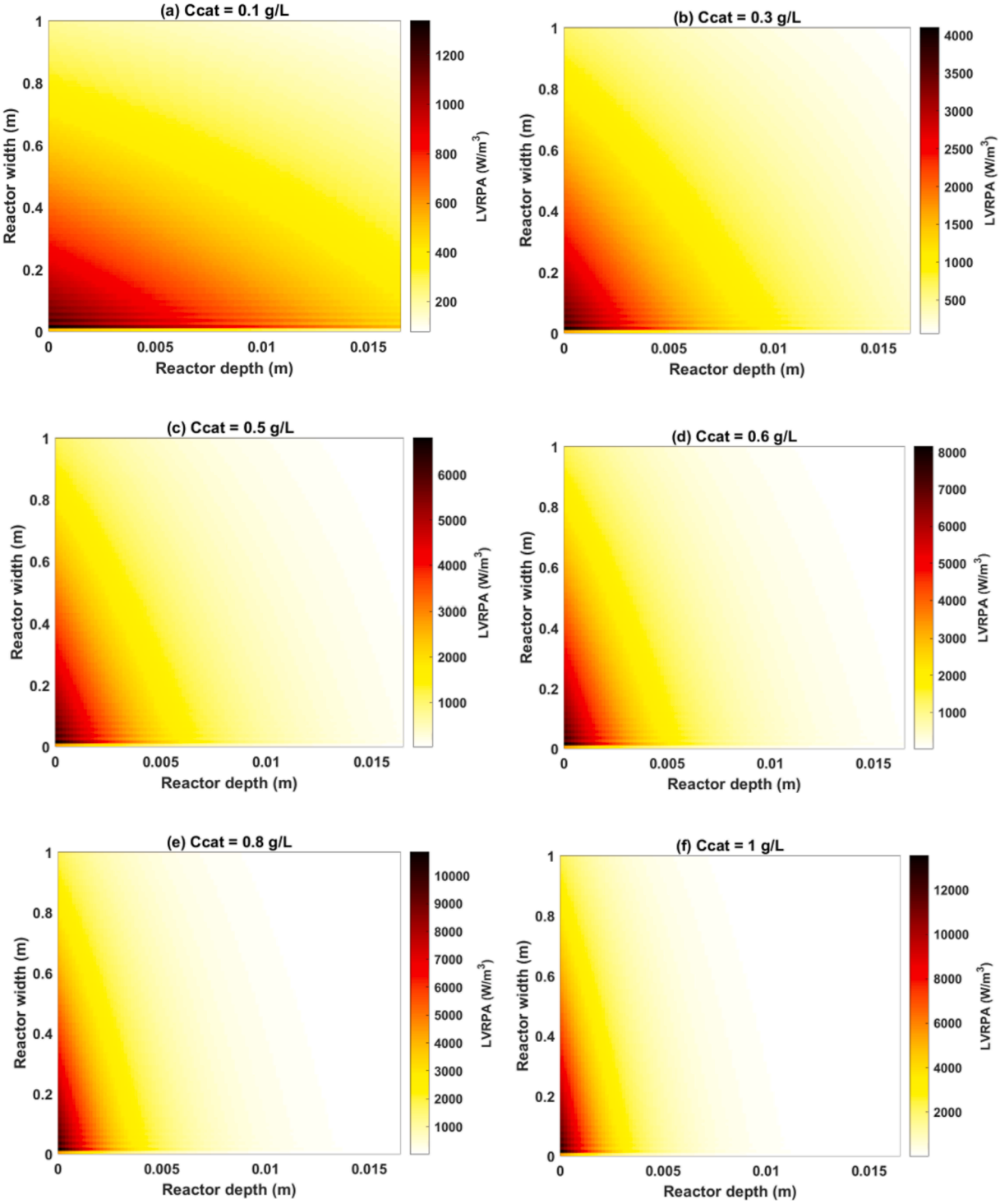

Fig. 7. Absorption profile in the reactor for different catalyst loading ($L_p = 0.0165$ m, $L = 1$ m).

significant increase is observed, no matter the increase in the reactor depth. Then, for any catalyst loading, it is possible to find the optimum reactor depth $L_{p,op}$ that corresponds to $VRPA_{op}$. In this study, $VRPA_{op}$ was arbitrarily taken as 99 % of the limit value of the *VRPA* when L_p approaches infinity, thus $L_{p,op}$ should verify Eq. (93).

$$VRPA_{op} = 0.99 \lim_{L_p \to +\infty} VRPA = \frac{\sqrt{A\alpha_0}L\left(j_0\left(e^{\sqrt{A\alpha_0}L_{p,op}} - 1\right) - l_0\left(e^{-\sqrt{A\alpha_0}L_{p,op}} - 1\right)\right)}{C_1 + C_2} + 2\sum_{n=1,n\ odd\ integer}^{+\infty}\left[\frac{L(A\alpha_n + \zeta n(1-\alpha_n))\left(j_n\left(e^{\sqrt{A\alpha_n}L_{p,op}} - 1\right) - l_n\left(e^{-\sqrt{A\alpha_n}L_{p,op}} - 1\right)\right)}{\sqrt{A\alpha_n}(C_1 + C_2)}\right] \quad (93)$$

Eq. (93) was solved using Newton-Raphson algorithm, and the solutions were the same in both cases when the incident radiation intensity was constant or varied. Table 4 shows for each catalyst loading the corresponding optimum reactor depth. The solution found led to an apparent optical thickness of 1.47, like that reported earlier in this study.

The SFM-2D was systematically derived from photon balances, leading to a set of six partial differential equations, which were solved with only one symmetry consideration. It can be easily shown that the obtained solution satisfies this set of equations. Moreover, the stability of the analytical solution is ensured; in fact, a slight perturbation in the boundary condition at $x = L_p$ (related to the optical depth) does not significantly affect the solution. This is evident in Figs. 9 and 10, where the *VRPA* asymptotically increases with L_p towards a fixed value with reactor depth for any catalyst loading.

3.2.4. Generalized criteria for the selection of the optimum reactor depth and catalyst loading for photocatalytic water decontamination

Each couple (C_{cat}, $L_{p,op}$) in Table 4 yields the same amount of radiation absorption (*VRPA*/Im = 0.49 m and 0.78 m) when the incident radiation intensity at the reactor boundary was constant or when it varied along the *y*-axis respectively. Thus, in principle, we could select any couple (C_{cat}, $L_{p,op}$) to obtain an optimum design that maximizes photon absorption in a photocatalytic slab. However, more insights are needed to understand which couple is more suitable to carry out photocatalytic water decontamination in a large-scale reactor. The first consideration is that the design should be made for a unit surface area of the front wall since the incident light is external to the reactor (e.g., sunlight or artificial light sources). The second consideration is that the reactor should be operated under turbulent flow conditions to obtain faster contaminants removal [28]; thus, in the absence of external mixing devices, the Reynolds number should be higher than 1400, and the maximum reactor depth can be determined for a required water treatment flowrate. Then, since photocatalytic reaction kinetics can be approximated as an apparent first-order reaction (deriving from an apparent Langmuir-Hinshelwood (L-H) rate law) [29], the larger the reactor volume, the higher the contaminant conversion for the same flowrate, thus, greater depths lead to larger reactor volumes for the same front wall area. However, the adsorption of the reactive species (e.g., the water contaminants and other species) over the catalyst should also be

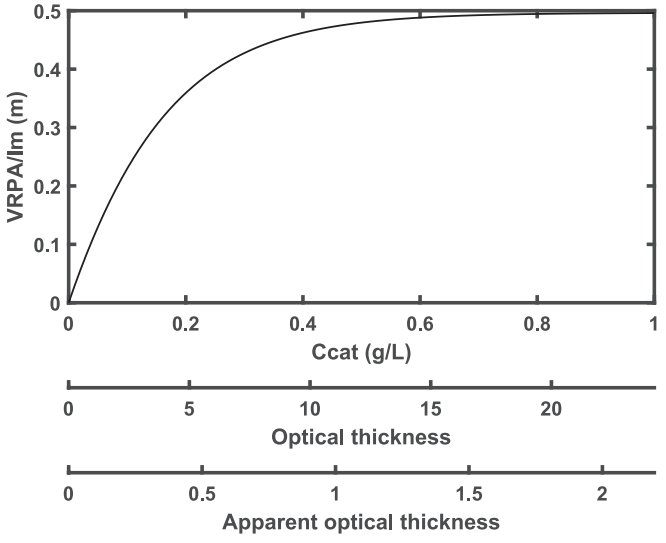

Fig. 8. The *VRPA* per unit of the irradiance measured at the reactor front wall vs catalyst loading, apparent optical thickness, and optical thickness (L_p = 0.0165 m, L = 1 m).

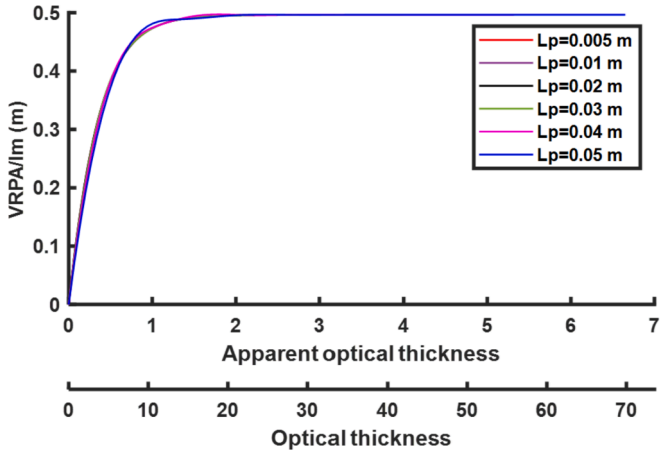

Fig. 9. The *VRPA* /Im as a function of τ and τ_{App2} with different reactor depths L_p and with catalyst parameters in Table 1.

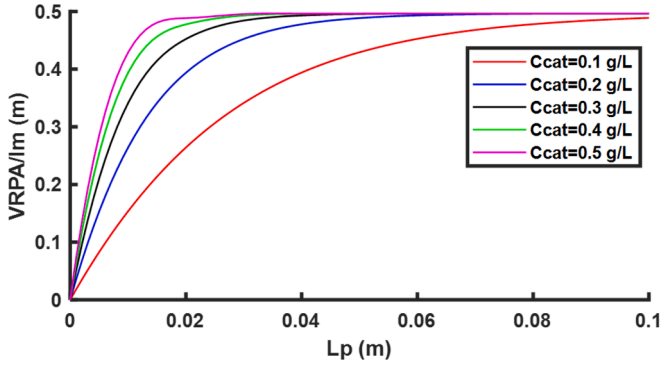

Fig. 10. The *VRPA* per unit of the irradiance measured at the reactor front wall vs the reactor depth at different catalyst loadings with variable intensity of incident radiation at the front wall.

Table 4
Optimum reactor depth at different catalyst loadings. Catalyst optical properties from Table 1.

C_{cat}(g/L)	$L_{p,op}$(cm)	τ_{App2}
0.1	11.04	1.47
0.2	5.52	1.47
0.3	3.68	1.47
0.4	2.76	1.47
0.5	2.21	1.47
0.6	1.84	1.47
0.7	1.58	1.47
0.8	1.38	1.47

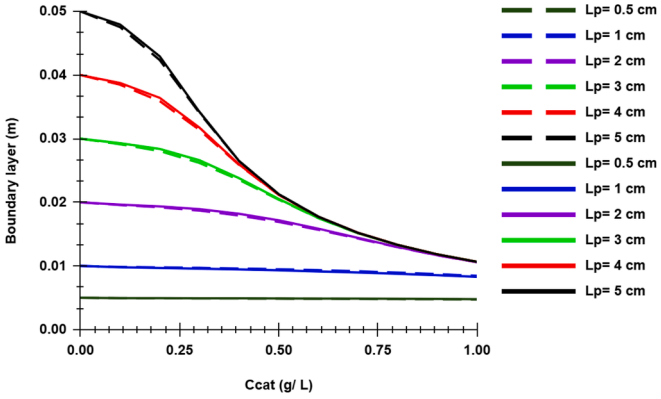

Fig. 11. The boundary layer of photon absorption as a function of catalyst loading for different reactor depths. Dashed and straight lines represent the SFM-2D with the incident radiation intensity constant and varying respectively for different reactor depths.

considered, meaning that at a high pollutant load a higher catalyst concentration should be required to handle the adsorption of contaminants on the catalyst surface sites, and at low pollutant load a lower catalyst concentration would be selected to adsorb all contaminants. Thus, the catalyst concentration that should be used in a slab reactor is determined by the ability of the photocatalyst to remove contaminants without achieving *complete saturation* of the catalyst active sites (for example, at very high pollutant loads). Considering that photocatalytic reactions have been described by an apparent Langmuir-Hinshelwood rate law [29],

$$-r_j = k(LVRPA)^m \frac{C_j}{1+\sum_{j=1}^{n} k_{ads,j} C_j} \tag{94}$$

with $m \leq 1$, the overall kinetic regime should therefore be maintained in the region between first and half-order ($1 \gg \sum_{j=1}^{n} k_{ads,j} C_j$) to avoid the saturation of the catalyst active sites. Once the catalyst concentration has been determined from well controlled laboratory scale reactors optimized according to the same criteria shown in Table 4 (for example using slit reactors with variable depths), then the optimum reactor depth for the large-scale reactor can be determined by applying the criteria of optimal τ or τ_{App2} described above.

Another approach to reactor sizing uses the concept of the "boundary layer of photon absorption", which has been presented as a helpful design parameter for slurry photoreactors with planar geometry [26]. Comparable to thermal, hydrodynamic, and mass boundary layers, the boundary layer of photon absorption is described as the reactor thickness δ_{abs} measured from the irradiated photoreactor surface, where 99% of the total energy is absorbed [26]. Beyond δ_{abs}, there is a *dark zone* in the reactor, i.e., no photon absorption. δ_{abs} is calculated from Eq. (95), which was solved using the Newton-Raphson algorithm.

$$\int_0^{\delta_{abs}} \int_0^{L} LVRPA dx dy = 0.99 VRPA \tag{95}$$

Fig. 11 displays the dependence of δ_{abs} on C_{cat} for different reactor depths for the boundary conditions with constant and variable incident radiation intensity. It was observed that for both cases, δ_{abs} decreases with increasing C_{cat} since at higher catalyst loading, photon penetration to the inner region of the reactor becomes more difficult. When the reactor depth is less than or equal to 1 cm or catalyst loading is less than 0.1 g/L, approximately, absorption takes place throughout practically the whole reactor; these results are consistent with the literature [26,30].

3.3. SFM-2D overall considerations

The model presented in this study includes conventional parameters used in photoreactor engineering, such as catalyst-specific absorption and scattering coefficients, scattering albedo, scattering phase function, reactor depth, optical thickness, apparent optical thickness, and catalyst loading [31]. Although a strict sensitivity analysis was not performed, the effect of each parameter on radiation absorption was evaluated. The focus was primarily on establishing a mathematical method that enables an accurate assessment of light behavior within photocatalytic reactors used in environmental applications and a model that is easy to apply in the design, sizing, and calculation of such process equipment [32]. As the model is an analytical solution, no error is expected. However, errors

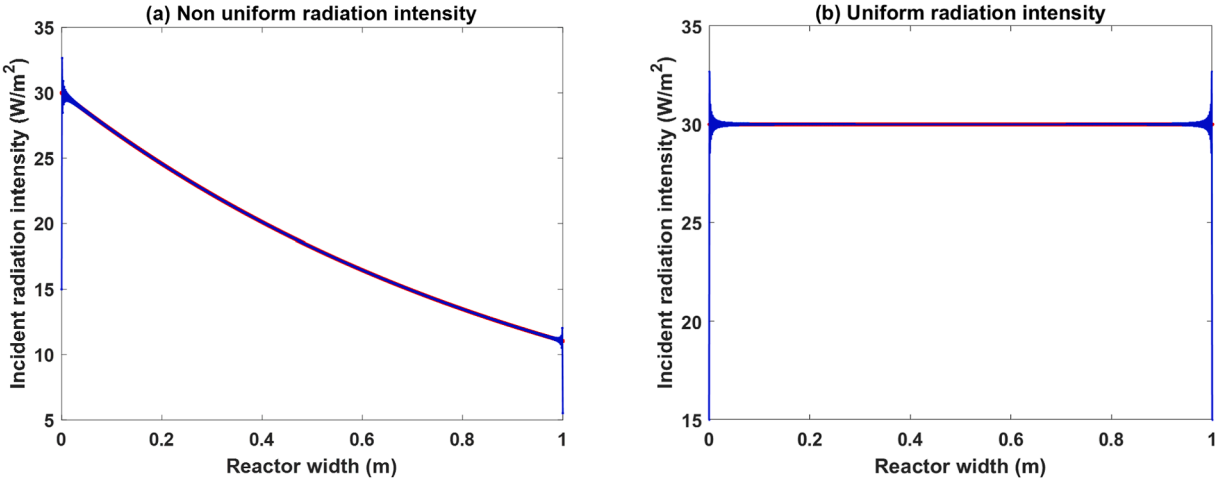

Fig. 12. Incident radiation models (red line) and their Fourier transform (blue line) versus reactor width.

may arise due to using the Fourier series for the boundary conditions. Nevertheless, Fig. 12 confirms that the incident radiation models defined in this work match their Fourier expansions, as they satisfy the Dirichlet conditions. Moreover, simulations were conducted using more than 1000 terms of the series, ensuring convergence. This implies that any errors resulting from using the Fourier series, if present, are negligible.

The scattering probability parameters of the model (f, b, and s) were derived from the original SFM formulation [12], which represents the possible photon paths within the process as described in the manuscript. Probability corrections have already been addressed in previous studies [20] and were also incorporated into this study. On the other hand, the model's predictive capability was demonstrated by evaluating its performance near the reactor walls under the simulated conditions. While the assumptions regarding scattering probabilities are inherent to the formulation, the model's validation confirmed its accuracy. The analysis of the impact of these assumptions on model performance was beyond the scope of this study.

As is well known, optical thickness is fundamental in photoreactor design analysis. However, the validity of the SFM-2D and its performance in near-wall regions exhibit behavior similar to that described by other mathematical approaches [23]. Moreover, this work emphasizes apparent optical thickness rather than optical thickness, as the former has been proven to be a more reliable design parameter. The simulations presented and the results obtained regarding apparent optical thickness are highly relevant to solar photoreactor engineering. Guidelines for the optimum design of photocatalytic reactors using the concept of apparent optical thickness have been reported [22]. The validation of the present model using more rigorous computational methods or computational packages that simulate radiant fields was not considered due to the transitivity principle. Since the current work formulates a model based on the SFM-1D, its validation was conducted through direct comparison with this model, which has already been rigorously validated using other methods and computational simulations [12]. Therefore, by applying the transitivity principle, the validity of the proposed model is justified. Nevertheless, future studies will consider direct validation of the SFM-2D using conventional rigorous methods such as DOM or Monte Carlo, although indirect validation has already been performed with both [11,33]. Additionally, in the context of heterogeneous photocatalytic reactors, no experimental validation data have been reported in the literature.

4. Conclusions

In this study, the RTE was solved in 2D in rectangular coordinates using the SFM approach to provide an estimation of the *LVRPA* and *VRPA* in flat slab photocatalytic reactors employing suspended photocatalytic particles. The model advances over the SFM-1D and allows the use of variable incident radiation at the reactor walls. The model incorporating the absorption of radiation by the suspended photocatalytic particles and by the fluid matrix, including all reactive species, allows the estimation of the optimum reactor depth and catalyst loading to maximize radiation adsorption, achieving complete irradiation of the entire reactor volume, thus avoiding dark zones. It was shown that the appropriate selection of the scattering phase function is crucial to obtain precise evaluations of radiation absorption in suspended photocatalysts. Moreover, a generalized criterion for the selection of the optimum reactor depth and catalyst loading for photocatalytic water decontamination was discussed, making also use of the dimensionless design parameters, including the reactor optical thickness τ and apparent optical thicknesses τ_{App2}. The solutions of the RTE with SFM-1D and SFM-2D were compared and discussed. The LVRPA profiles calculated with the SFM-2D and the SFM-HG matched closely in the region near the slab front wall where the incident radiation source enters the reactor, but were significantly different in the regions far away from it. For TiO_2-P25 and solar irradiation, it was shown that optimal radiation absorption in the slab is obtained for $\tau = 16.3$ and $\tau_{App2} = 1.47$. The SFM-2D model can be useful not only for the estimation of the radiant field in slab photocatalytic reactors but also for other photochemical processes carried out in a slab geometry where solving the RTE is needed and where the medium does not emit radiation. Overall, the SFM-2D provides a more accurate optimization of the radiation field in a flat plate with non-uniform irradiation of the front wall, allowing a more accurate estimation of the optimum catalyst load and slab thickness, thus facilitating the design of photocatalytic reactors with suspended photocatalysts.

CRediT authorship contribution statement

Clovis Nchikou: Writing – original draft, Validation, Software, Methodology, Investigation, Conceptualization. **José Ángel Loredo-Medrano:** Project administration. **Aracely Hernández-Ramírez:** Supervision, Resources, Project administration. **José Ángel Colina-Marquez:** Project administration. **Miguel Ángel Mueses:** Writing – original draft, Visualization, Validation, Supervision, Resources, Project administration, Methodology, Investigation, Funding acquisition, Formal analysis, Conceptualization. **Gianluca Li Puma:** Writing – review & editing, Writing – original draft, Validation, Methodology, Conceptualization.

Declaration of competing interest

The authors declare the following financial interests/personal relationships which may be considered as potential competing interests: [G. Li Puma has served/is serving as Guest Editor of a Special Issue for Chemical Engineering Journal. If there are other authors, they declare that they have no known competing financial interests or personal relationships that could have appeared to influence the work reported in this paper].

Acknowledgements

The authors thank Universidad Autónoma de Nuevo León and Universidad de Cartagena for supporting this publication. Prof. Mueses thanks funding from Grant 031-2022 (Research Vice-Head) of the University of Cartagena. The authors dedicate this article to the memory of Dr. Juan-Antonio Rojas-Estrada and Professor Dionysios (Dion) Dionysiou, who were recently missed among the scientific community.

Appendix A. Supplementary data

Supplementary data to this article can be found online at https://doi.org/10.1016/j.cej.2025.163102.

Data availability

Data will be made available on request.

References

[1] C. Byrne, G. Subramanian, S.C. Pillai, Recent advances in photocatalysis for environmental applications, J. Environ. Chem. Eng. 6 (3) (2018) 3531–3555, https://doi.org/10.1016/j.jece.2017.07.080.
[2] B.M. da Costa Filho, V.J.P. Vilar, Strategies for the intensification of photocatalytic oxidation processes towards air streams decontamination: A review, Chem. Eng. J. 391 (2020) 123531, https://doi.org/10.1016/j.cej.2019.123531.
[3] S.K. Lakhera, A. Rajan, N. Bernaurdshaw, A review on particulate photocatalytic hydrogen production system: Progress made in achieving high energy conversion efficiency and key challenges ahead, Renew. Sustain. Energy Rev. 152 (2021) 111694, https://doi.org/10.1016/j.rser.2021.111694.
[4] S. Hamdan, K. Al-Ali, L.F. Vega, M. Muscetta, A.O. Yusuf, G. Palmisano, Zinc cadmium sulphide (ZnxCd1-xS)-based photocatalysts for hydrogen production from seawater and wastewater, J. Environ. Chem. Eng. 12 (5) (2024) 113937, https://doi.org/10.1016/j.jece.2024.113937.
[5] M. Bellardita, V. Loddo, L. Palmisano, Formation of High Added Value Chemicals by Photocatalytic Treatment of Biomass, Mini-Rev. Org. Chem. 17 (7) (2020) 884–901, https://doi.org/10.2174/1570193x17666200131112856.

[6] R. Molinari, C. Lavorato, P. Argurio, Visible-Light Photocatalysts and Their Perspectives for Building Photocatalytic Membrane Reactors for Various Liquid Phase Chemical Conversions, Catalysts 10 (11) (2020) 1334, https://doi.org/10.3390/catal10111334.
[7] Schneider, J., Bahnemann, D., Ye, J., Li Puma, G., & Dionysiou, D. D. (Eds.). (2016). Photocatalysis. Energy and Environment Series. https://doi.org/10.1039/9781782622338.
[8] A.E. Cassano, O.M. Alfano, Reaction engineering of suspended solid heterogeneous photocatalytic reactors, Catal. Today 58 (2–3) (2000) 167–197, https://doi.org/10.1016/s0920-5861(00)00251-0.
[9] J.R. Howell, M.P. Mengüç, K. Daun, R. Siegel, Thermal Radiation Heat Transfer, CRC Press (2020), https://doi.org/10.1201/9780429327308.
[10] D. Joseph, P. Perez, M. El Hafi, B. Cuenot, Discrete Ordinates and Monte Carlo Methods for Radiative Transfer Simulation Applied to Computational Fluid Dynamics Combustion Modeling, J. Heat Transfer 131 (5) (2009), https://doi.org/10.1115/1.3013832.
[11] P.M. Moreira, G. Li Puma, Multiphysics Computational Fluid-Dynamics (CFD) Modeling of Annular Photocatalytic Reactors by the Discrete Ordinates Method (DOM) and the Six-Flux Model (SFM) and Evaluation of the Contaminant Intrinsic Kinetics Constants, Catal. Today 361 (2021) 77–84, https://doi.org/10.1016/j.cattod.2020.01.012.
[12] Brucato, A., Cassano, A. E., Grisafi, F., Montante, G., Rizzuti, L., & Vella, G. (2006). Estimating radiant fields in flat heterogeneous photoreactors by the six-flux model. AIChE Journal, 52(11), 3882–3890. Portico. https://doi.org/10.1002/aic.10984.
[13] J. Colina-Márquez, F. Machuca-Martínez, G.L. Puma, Radiation Absorption and Optimization of Solar Photocatalytic Reactors for Environmental Applications, Environ. Sci. Tech. 44 (13) (2010) 5112–5120, https://doi.org/10.1021/es100130h.
[14] J. Diaz-Angulo, J. Lara-Ramos, M. Mueses, A. Hernández-Ramírez, G. Li Puma, F. Machuca-Martínez, Enhancement of the oxidative removal of diclofenac and of the TiO2 rate of photon absorption in dye-sensitized solar pilot scale CPC photocatalytic reactors, Chem. Eng. J. 381 (2020) 122520, https://doi.org/10.1016/j.cej.2019.122520.
[15] W.H. Saputera, J.J. Pranata, R. Jonatan, P. Widiatmoko, D. Sasongko, Photocatalytic Simulation of Phenol Waste Degradation Using Titanium Dioxide (TiO2) P25-Based Photocatalysts, Journal of Engineering and Technological Sciences 55 (4) (2023) 419–433, https://doi.org/10.5614/j.eng.technol.sci.2023.55.4.6.
[16] S. Kuharat, O. Anwar Bég, A. Kadir, B. Vasu, Computation of Metallic Nanofluid Natural Convection in a Two-Dimensional Solar Enclosure with Radiative Heat Transfer, Aspect Ratio and Volume Fraction Effects, Arab. J. Sci. Eng. 45 (11) (2020) 9075–9093, https://doi.org/10.1007/s13369-020-04678-1.
[17] M.A. Ramírez-Cabrera, P.J. Valadés-Pelayo, C.A. Arancibia-Bulnes, E. Ramos, Validity of the Six-Flux model for photoreactors, Chem. Eng. J. 330 (2017) 272–280, https://doi.org/10.1016/j.cej.2017.07.120.
[18] M.L.R. Peixoto, M.S.C.A. Brito, R.J. Santos, V.J.P. Vilar, Kinetic model implementation in raceway pond reactors with hydrodynamic and radiation fields, Chem. Eng. Res. Des. 210 (2024) 150–162, https://doi.org/10.1016/j.cherd.2024.08.030.
[19] C. Inostroza, A. Solimeno, J. García, J.M. Fernández-Sevilla, F.G. Acién, Improvement of real-scale raceway bioreactors for microalgae production using Computational Fluid Dynamics (CFD), Algal Res. 54 (2021) 102207, https://doi.org/10.1016/j.algal.2021.102207.
[20] R. Acosta-Herazo, J. Monterroza-Romero, M.Á. Mueses, F. Machuca-Martínez, G. Li Puma, Coupling the Six Flux Absorption–Scattering Model to the Henyey–Greenstein scattering phase function: Evaluation and optimization of radiation absorption in solar heterogeneous photoreactors, Chem. Eng. J. 302 (2016) 86–96, https://doi.org/10.1016/j.cej.2016.04.127.
[21] M.A. Mueses, F. Machuca-Martinez, A. Hernández-Ramirez, G. Li Puma, Effective radiation field model to scattering – Absorption applied in heterogeneous photocatalytic reactors, Chem. Eng. J. 279 (2015) 442–451, https://doi.org/10.1016/j.cej.2015.05.056.
[22] D. Wang, M.A. Mueses, J.A.C. Márquez, F. Machuca-Martínez, I. Grčić, P. M. Moreira, G. Li Puma, Engineering and modeling perspectives on photocatalytic reactors for water treatment, Water Res. 202 (2021) 117421, https://doi.org/10.1016/j.watres.2021.117421.
[23] C. Nchikou, J.Á. Loredo-Medrano, A. Hernández-Ramírez, J.Á. Colina-Marquez, M.Á. Mueses, Estimation of the radiation field for CPC photocatalytic reactors using a novel six-flux model in two dimensions (SFM-2D), J. Environ. Chem. Eng. 9 (6) (2021) 106392, https://doi.org/10.1016/j.jece.2021.106392.
[24] G. Li puma, Dimensionless Analysis of Photocatalytic Reactors Using Suspended Solid Photocatalysts, Chem. Eng. Res. Des. 83 (7) (2005) 820–826, https://doi.org/10.1205/cherd.04336.
[25] J. Colina-Márquez, F. Machuca-Martínez, G. Li Puma, Photocatalytic Mineralization of Commercial Herbicides in a Pilot-Scale Solar CPC Reactor: Photoreactor Modeling and Reaction Kinetics Constants Independent of Radiation Field, Environ. Sci. Tech. 43 (23) (2009) 8953–8960, https://doi.org/10.1021/es902004b.
[26] H.L. Otálvaro-Marín, M.A. Mueses, F. Machuca-Martínez, Boundary layer of photon absorption applied to heterogeneous photocatalytic solar flat plate reactor design, Int. J. Photoenergy (2014) 1–8, https://doi.org/10.1155/2014/930439.
[27] R.J. Brandi, O.M. Alfano, A.E. Cassano, Modeling of radiation absorption in a flat plate photocatalytic reactor, Chem. Eng. Sci. 51 (1996) 3169–3174, https://doi.org/10.1016/0009-2509(96)00215-1.
[28] G. Li Puma, Modeling of thin-film slurry photocatalytic reactors affected by radiation scattering, Environ. Sci. Tech. 37 (2003) 5783–5791, https://doi.org/10.1021/es0300362.
[29] C.S. Turchi, D.F. Ollis, Photocatalytic degradation of organic water contaminants: Mechanisms involving hydroxyl radical attack, J. Catal. 122 (1990) 178–192, https://doi.org/10.1016/0021-9517(90)90269-p.
[30] R. Acosta-Herazo, M.A. Mueses, G. Li Puma, F. Machuca-Martínez, Impact of photocatalyst optical properties on the efficiency of solar photocatalytic reactors rationalized by the concepts of initial rate of photon absorption (IRPA) dimensionless boundary layer of photon absorption and apparent optical thickness, Chemical Engineering Journal 356 (2019) 839–849, https://doi.org/10.1016/j.cej.2018.09.085.
[31] E.O. Ichipi, R. Mugumo, S.M. Tichapondwa, E.M.N. Chirwa, A comparative study of metal-sulphide/ZnO for visible-light-induced photocatalysis and the six-flux photon absorption model of an external lamp photoreactor, J. Environ. Chem. Eng. 12 (5) (2024) 113355, https://doi.org/10.1016/j.jece.2024.113355.
[32] D. Olivo-Alanís, A. García-González, M.A. Mueses, R.B. García-Reyes, Generalized kinetic model for the photocatalytic degradation processes: Validation for dye wastewater treatment in a visible-LED tubular reactor, Appl Catal B 317 (2022) 121804, https://doi.org/10.1016/j.apcatb.2022.121804.
[33] J. Akach, A. Ochieng, Monte Carlo simulation of the light distribution in an annular slurry bubble column photocatalytic reactor, Chem. Eng. Res. Des. 129 (2018) 248–258, https://doi.org/10.1016/j.cherd.2017.11.021.